FIELD ANALYSIS OF DIELECTRIC WAVEGUIDE DEVICES BASED ON COUPLED TRANSVERSE-MODE INTEGRAL EQUATION — NUMERICAL INVESTIGATION

H.-W. Chang, Y.-H. Wu, S.-M. Lu, and W.-C. Cheng

Institute of Electro-optical Engineering and Department of Photonics
National Sun Yat-sen University
Kaohsiung 80424, Taiwan

M.-H. Sheng

Department of Management Information Science
Chia Nan University of Pharmacy & Science
Tainan 71710, Taiwan

Abstract—This is a numerical investigation of a recently proposed formulation called coupled transverse-mode integral equation (CTMIE) for analyzing EM field properties in general 2-D dielectric waveguide devices. The device is first approximated by stack of piece-wise 1-D horizontally layered structures. Transverse field components on the interface between waveguide slices are unknown functions, which are governed by a coupled integral equation. When unknowns are expanded as a linear combination of given functions, CTMIE is converted to a coupled block matrix equation. We study three waveguide devices, in detail, to understand the relation between modeling parameters and accuracy and convergent rate of the solutions. Examples include a step waveguide junction, a multi-mode interferometer power cross coupler and a linearly tapered waveguide. All results are verified with independent calculations using other proven methods.

1. INTRODUCTION

Passive dielectric waveguides devices are important building blocks in modern optical communication systems [1, 2]. 2-D dielectric waveguide problems are divided into TE and TM cases. The two cases are

---

Corresponding author: H.-W. Chang (hchang@faculty.nsysu.edu.tw).

decoupled and can each be treated as a scalar wave problem [3, 4]. For complex but compact optical devices, full wave methods such as the finite-difference time-domain methods (FD-TD) [5], frequency-domain finite-difference methods (FD-FD) [6–8] and the finite element method [9] can be quite effective. For very large waveguides the beam propagation method (BPM) and its variations, FFT-BPM [1], FD-BPM [11] are used for studying field evolutions in a slowly varying waveguide and for mode profile determination in a 3-D straight waveguide. BPM is the only available option for modeling large complex 3D waveguide devices.

For obtaining highly accurate, full-wave analysis of complex medium-size waveguide devices we proposed a rigorous CTMIE formulation [12]. In CTMIE the unknowns are the transverse field components between the slice interfaces. They satisfy a coupled integral equation which is derived in [12]. This paper handles numerical aspects of CTMIE method, including the choice of suitable basis function (auxiliary function), the effect on placement of two perfectly conducting walls and determination of the slicing density for devices with continuously varying profiles. Our CTMIE method is closely related to the mode-matching method [13] and film mode-matching [14]. It is the scalar version of the much more complex, "vectorial" VCTMIE [15, 16] formulation designed for computing full-wave, transverse modes of constant profile 3-D dielectric waveguides.

This paper is focused on numerical aspects of CTMIE method, including the accuracy convergent speed and required computer resources as functions of various CTMIE parameters. To meet these purposes, we will investigate in detail the following three waveguide examples: a dielectric waveguide with a step discontinuity, a power cross coupler based on the multi-mode interferometer and a 45 degree linearly tapered waveguide. We will discuss how to tune of CTMIE modeling parameters to obtain the solutions with minimum computational effort. We verify the convergence of the solutions with results computed by our hybrid FD-FD method [8] or by running separate CTMIE calculations with or without considering the problem symmetry. All cases are checked and verified for both TE and TM polarizations.

2. CTMIE THEORY

We begin with the summary of the important results from our first paper [12]. A general 2-D (x, z) dielectric waveguide device is shown in Figure 1. The device is divided into $N + 1$ sections by a series of vertical cuts. Each section, called a slice, is then approximated by a
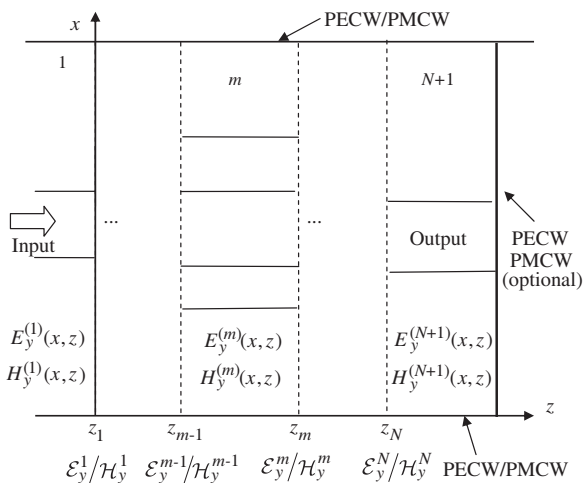
Figure 1. A general 2-D (x, z) dielectric waveguide device is divided into $N + 1$ vertical slices made of a 1-D horizontally multilayer waveguide embedded in a pair of PECWs/PMCWs. Input waveguide is the first slice and, in the absence of the right PECW/PMCW, the output waveguide in the last $(N+1)$ slice. Under CTMIE formulation, the unknowns are 1-D function, $\{\mathcal{E}_y^m(x)/\mathcal{H}_y^m(x)\}$, $m = 1, \ldots, N$ on the interfaces between two adjacent slices for TE/TM polarization.

"closest" 1-D horizontal layered waveguide. The input waveguide is on the left while the exit waveguide is on the right. CTMIE requires that both input and output waveguide be horizontally stratified.

The spectrum of an open multilayer waveguide is made of a finite number of guided modes and an infinite number of continuous radiation modes. To discretize the radiating modes, we place two perfectly electric/magnetic conducting walls (PECWs/PMCWs) [17] at the top and bottom boundaries far away from the guiding core. In the last region, the exit waveguide may continue to infinity or be terminated by a PECW or a PMCW.

We next consider the functional relations among the four tangential field components located at the two ends, at $z = z_{m-1}$ and $z = z_m$ of slice m. Figure 2 illustrates the physical significance of the four Green's integral operators for this slice. Assuming a TM polarization, we have $\mathbf{P}_h^{(m)}(x, x')$ operator that propagates and transforms the $\mathcal{H}_y^{m-1}(x')$ function into $\mathcal{E}_x^m(x)$. Operator $\mathbf{Q}_h^{(m)}(x, x')$ performs a "back reflection" and transforms the right interface function $\mathcal{H}_y^m(x')$ into its dual EM component $\mathcal{E}_x^m(x)$. Similarly, operator
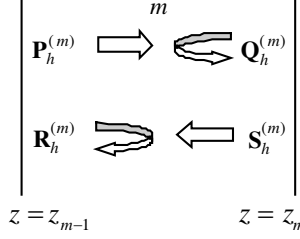
Figure 2. P Q R S Green's operators within the mth slice.

$\mathbf{R}_h^{(m)}(x, x')$ represents "reflection onto itself" and takes the left-side functions $\mathcal{H}_y^{m-1}(x')$ to its dual EM component $\mathcal{E}_x^{m-1}(x)$. Finally $\mathbf{S}_h^{(m)}(x, x')$ propagates, in reverse, and maps the right unknown function $\mathcal{H}_y^m(x')$ to the left target function $\mathcal{E}_x^{m-1}(x)$. Note that errors in our first theoretical paper as well as the changes in definitions of $\mathbf{Q}$ and $\mathbf{R}$ operators are corrected in this paper [18] and so are the drawing of Figure 2.

Using these four operators, we may express the two transverse electric field functions (on the two ends of the mth slice) in terms of the two unknown magnetic field functions. Dropping the x/y subscripts, we arrive at the main integral operators as follow

$$
\begin{aligned}
\mathcal{E}_{m-1}(x) = \int \mathbf{R}_h^{(m)} \mathcal{H}_{m-1}(x') dx' + \int \mathbf{S}_h^{(m)} \mathcal{H}_m(x') dx', \\
\mathcal{E}_m(x) = \int \mathbf{P}_h^{(m)} \mathcal{H}_{m-1}(x') dx' + \int \mathbf{Q}_h^{(m)} \mathcal{H}_m(x') dx'.
\end{aligned}
\tag{1}
$$

With Equation (1) we know how to calculate all the transverse electric field components on each interface between two adjacent slices. Since the transverse magnetic field component $\mathcal{H}_{m-1}(x)$ is shared with slice $m - 1$ and slice m, all tangential magnetic field components are automatically continuous. We must also require that all tangential electric field components $\{\mathcal{E}_m(x)\}$ be continuous across the slice interface. These $\mathcal{E}_m(x)$ field components are generated from $\mathcal{H}_m(x)$. Thus we have the following block tri-diagonal coupled integral equation for these $\mathcal{H}_m(x)$ to obey:

$$
\int dx' \begin{bmatrix} \mathbf{G}_{1,1} & \mathbf{G}_{1,2} & 0 & \cdots & & 0 \\ \vdots & \ddots & \vdots & \cdots & & 0 \\ \cdots & \cdots & \mathbf{G}_{i,i} & \cdots & & 0 \\ \vdots & \vdots & \vdots & \ddots & & \vdots \\ 0 & \cdots & 0 & \mathbf{G}_{N,N-1} & \mathbf{G}_{N,N} \end{bmatrix} \begin{bmatrix} \mathcal{H}_1 \\ \vdots \\ \mathcal{H}_i \\ \vdots \\ \mathcal{H}_N \end{bmatrix} = \begin{bmatrix} 2\mathcal{E}_{\text{inc}} \\ \vdots \\ 0 \\ \vdots \\ 0 \end{bmatrix}
\tag{2}
$$

Each matrix element is an operator given by

$$\mathbf{G}_{1,1} = \mathbf{R}_h^{(1)} - \mathbf{Q}_h^{(2)}, \mathbf{G}_{1,2} = -\mathbf{S}_h^{(2)}$$
$$\mathbf{G}_{i,i-1} = \mathbf{P}_h^{(i)}, \mathbf{G}_{i,i} = \mathbf{R}_h^{(i)} - \mathbf{Q}_h^{(i+1)}, \mathbf{G}_{i,i+1} = -\mathbf{S}_h^{(i+1)}, \qquad (3)$$
$$\mathbf{G}_{N,N-1} = \mathbf{P}_h^{(N)}, \mathbf{G}_{N,N} = \mathbf{R}_h^{(N)} - \mathbf{Q}_h^{(N+1)},$$

where $i = 1, \ldots, N - 1$. It is noted that $-\mathbf{S}_h^{(i)} = \mathbf{P}_h^{(i)}$ and $\mathbf{G}_{i,i+1} = \mathbf{G}_{i+1,i}$. Interested readers should referred to [12] for detail definitions of these operators. Equations (1)–(3) are for TM cases. TE cases follow in a similar way if we first replace all 2-D functions $H_y(x, z)$ and $E_x(x, z)$ by $E_y(x, z)$ and $H_x(x, z)$, respectively, then we substitute $\mathcal{H}_m(x)$ by $\mathcal{E}_m(x), \epsilon(x)$ with μ_0 and finally, TM admittance by TE admittance.

To obtain numerical solutions, we need to convert Equation (2) into a matrix equation. This is done by expressing $\{\mathcal{E}_m(x)\}$ or $\{\mathcal{H}_m(x)\}$ as linear combination of some known functions (also called auxiliary functions). Consider the TM case, let N_b be the number of terms used to expand the unknown tangential field $\mathcal{H}_m(x)$, we write

$$\mathcal{H}_m(x) \cong \sum_{n=1}^{N_b} c_n^{(m)} \varphi_n^{(m)}(x), \quad m = 1, \ldots, N. \qquad (4)$$

To proceed further, we also need the overlap integrals between the ith function $\mathcal{H}_i(x)$ and slice mode functions of region $j = i$ or $j = i+1$. They are given by

$$O^{\bar{i},j} = \left[O_{k,l}^{\bar{i},j} \right] = \left(O^{j,\bar{i}} \right)^T$$
$$O_{k,l}^{\bar{i},j} \triangleq \int \varphi_k^{(i)}(x) \frac{1}{\epsilon_r^{(j)}(x)} \phi_l^{(j)}(x) \, dx, \qquad (5)$$
$$O_{k,l}^{j,\bar{i}} \triangleq \int \phi_k^{(j)}(x) \frac{1}{\epsilon_r^{(j)}(x)} \varphi_l^{(i)}(x) \, dx = O_{l,k}^{\bar{i},j}.$$

The bar resting on top of i, j superscripts is for denoting the position of the auxiliary function while indices without bars are for location of slice mode functions.

Auxiliary functions are usually chosen from orthonormal basis functions, for example, TE modes of some multi-layer structure or eigenfunctions from continuous index profile with exactly solvable permittivity $\epsilon(x)$ [19, 20]. All our numerical results are computed from using three different type (called AFtype) of Auxiliary functions. Given below, they are simple trigonometric bases (TB), the left (to the

interface) layermode bases (LB) and the right layermode bases (RB).

$$
\varphi_n^{(m)}(x) = \left\{
\begin{array}{ll}
\sqrt{\frac{a_n}{L}} \left\{ \begin{array}{l} \sin\left(n\pi x/L\right), \\ \cos\left[(n-1)\pi x/L\right], \end{array} \right. & \text{(TB)} \\
\phi_n^{(m-1)}(x), & \text{(LB)} \\
\phi_n^{(m)}(x), & \text{(RB)}
\end{array}
\right. , \quad n = 1, \ldots, N_b. \quad (6)
$$

The normalization factor $a_n = 2$ except when $n = 1$, $a_n = 1$. For comparison, mode matching method has either an AFtype = LB or AFtype = RB built-in.

For CTMIE, each type of auxiliary function has its own advantages and disadvantages. TB is most faithful basis but it requires more terms than others. When transmitted energy dominates the solution RB auxiliary function requires fewer terms than LB and thus converges faster.

3. RESULTS AND DISCUSSION

For numerical verification of CTMIE formulation, we show three examples corresponding to three total number of unknown slice interfaces, i.e., $N = 1, N = 2$ and $N \geq 3$ cases. For a single interface, we consider a dielectric slab waveguide with a step discontinuity. For the twointerface case, we study a two by two power cross coupler based on the multi-mode interferometer. Finally a 45 degree linearly tapered slab waveguide is investigated for representing a complex waveguide device that must be approximated by more than three slices.

The control parameters of CTMIE are (a) WD: distance between two artificial PECW/PMCW boundaries, (b) AFtype: type of auxiliary functions, in Equations (4) and (5), (c) N_{AF}: total number of AF terms for each unknown field function on each slice interface, (d) N_{SM}: total number of slice modes in each slice region and (e) D_{sl}: slicing density for continuous changing waveguide devices.

Since N_{AF} and N_{SM} are "proportional" to the wall distance, we define SMF (as the slice mode factor) and AFF (as the auxiliary function mode factor) to be independent of WD factor. By fixing SMF/AFF we apply automatic scaling of N_{AF} and N_{SM} in linear proportion to the WD factor. In FD-FD method, we define the grid sampling density parameter N_λ to be the number of grid point per wavelength inside the highest index region of the device. We normally choose $N_\lambda = 20 \sim 40$ to reduce numerical grid dispersion even though $N_\lambda = 2$ is the theoretical Nyquist limit for 1-D problem. AFF and SMF are the analog equivalent to N_λ.

Let us define M_{SM} to be total number of slice modes with real propagation constant and M_{AF} to be total number of AF

modes/functions that supports real propagation constant. Then the mode-density parameters, SMF and AFF can be written as:

$$F_{SM} = N_{SM}/M_{SM}, \quad F_{AF} = N_{AF}/M_{AF}. \tag{7}$$

Since all propagating modes propagate without any decay in amplitude, CTMIE always uses $F_{SM} \geq 3F_{AF}$ and $F_{AF} \geq 2$ to include all propagation modes and to capture the excited evanescent field at any discontinuity in a given problem. For comparison, in the 1-D FD-FD simulation with a $N_\lambda = 20$ will have an equivalent $F_{SM} = 10$ in CTMIE analysis which is considered a very large number.

3.1. Slab Waveguide with a Step Discontinuity

In this example, we choose our slab waveguide with a large index contrast between the core, made of siliconoxinitride, (SiNOx $n_{cor} = 2.5$) and air cladding ($n_{cld} = 1$). Such a high index contrast serves to enhance the field differences due to different polarization. Devices with high index contrast are also numerically, more challenging. This step waveguide has an input core thickness of $1\,\mu m$ and is suddenly reduced to $0.25\,\mu m$ at the junction. In Figure 3(a), we plot the 2-D TE $E_y(x, z)$ complex field amplitude near the junction when excited by the fundamental mode incident from the left, with a carrier wavelength $\lambda = 1.3\,\mu m$. The TM $H_y(x, z)$ distribution is plotted in Figure 3(b). These wave fields are symmetric with respect to the z-axis. To plot complex fields, we plot real parts of the fields in the upper halves of waveguides and the imaginary parts in the lower halves. Since there is a 90 degree phase difference between the real and the imaginary part of a propagating plane wave and no phase difference in a standing wave, we can better "visualize" symmetric complex fields this way. EM theory requires that tangential field components $E_y(x, z)$ and $H_y(x, z)$ be continuous across core-cladding boundary. The high resolution CTMIE simulations allow us to verify this fact by visual examination of the two figures. We also notice that TM field is significantly more confined in the core than TE field. This is because while normal derivative of $E_y(x, z)$ is continuous everywhere, it is the normal derivative of $H_y(x, z)$ divided by squared index, $n^2(x, z)$, need to be continuous across core-cladding interface and hence the TM field has a sharper slope near the air-core interface.

Numerical verification of CTMIE calculation for a low index contrast ($n_{cor} : n_{cld} = 3.5 : 3.2$) slab waveguide terminated in free space was first reported in 2001 [21]. The calculated reflected powers agree with previously published results using various approximations. We also showed that CTMIE could be applied to a much wider range of waveguide junction parameters.

Figures 3(a) and (b) are computed with CTMIE parameters $WD = 40\,\mu\text{m}$, $F_{\text{SM}} = 16$ and $F_{\text{AF}} = 4$. Also we choose AFtype to be TB so that we will obtain an "unbiased" solution of the junction field. We could have used fewer terms by choosing other auxiliary functions like guiding modes from a largecore highindex slab waveguide [21]. When comparing the field images with those computed by the hybrid FD-FD method [8] with a $N_\lambda = 30$ (not shown), we find that CTMIE images posses same features (resolution, smoothness, etc.) as those obtained by FD-FD method.

To quantitatively investigate the complex field of this step junction device, we compute the reflection and transmission coefficients of both guided and radiating power in the two waveguide regions: r_G, t_G and r_R, t_R. Lower case letter r/t stands for reflection/transmission power while capitalized subscript letter G/R indicates whether it is guided or radiating energy. The input waveguide supports four guided modes and the output waveguide has just one guided mode. Thus, r_G contains the sum of all four guided mode power reflected back to the input waveguide whereas t_G contains only the fundamental mode power in the output waveguide. A closer investigation of Figures 3(a) and (b), we see that there is a 90 degree phase difference in the real and imaginary part of the core field in the exit waveguide, a clear indication of a propagating wave field. The phase and the shape differences in the reflected guided power are much more complex due to multiple mode interference.
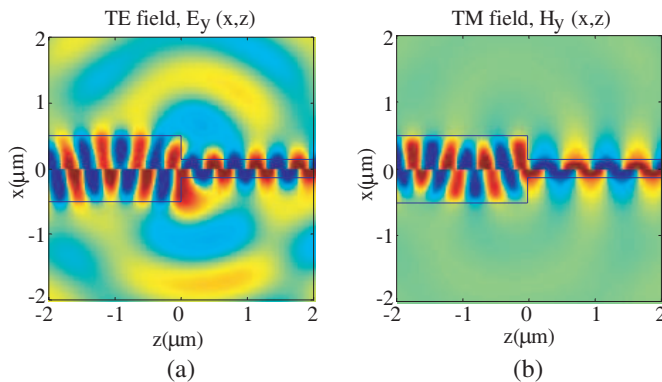
Figure 3. TE and TM field distributions near the step junction a symmetric dielectric slab waveguide due to a fundamental incident mode incident from the left. The core-cladding boundary marked by the blue line Real part is shown in the upper half of the waveguide and the imaginary part in the lower half.

As we will soon see that we are able to reduce the WD effect by computing each problem using an average of two independent simulations, namely,

$$u(x, z) = \frac{1}{2} \left[u^{\text{PECW}}(x, z) + u^{\text{PMCW}}(x, z) \right]. \qquad (8)$$

Quantitative power coefficients computed using Equation (8) are tabulated in Table 1 for both TE and TM polarization. For comparison, we also include results from the hybrid FD-FD method. Data show that r_G and t_G are within a few percent of relative error, while small quantities such as r_R and t_R differs by less than ten percents between the two methods.

Next, we consider the WD parameter, the effect of wall separation. We pick t_G as the quantity of interest since it is the dominate power coefficient. In Figure 4, we show fluctuating behavior of TE polarized, t_G as function of WD. Each data point is computed twice to form an average using Equation (8). We also set $F_{\text{SM}} = 25$, $F_{\text{AF}} = 5$ to keep the mode density sufficiently high. And as before we choose simple sinusoidal functions, AFtype = TB, to expand the unknown field junctions. The TM case is plotted in Figure 5 showing similar behavior. It is interesting to note that we can reduce the fluctuation of WD effect by taking the average of two opposite wall types. Normally, in a straight waveguide the guided power shall not be affected by the two far-away walls. In this step junction example, the sudden change of waveguide core thickness causes scattering and mixing between guided mode and radiated field bouncing off the two PECWs/PMCWs.
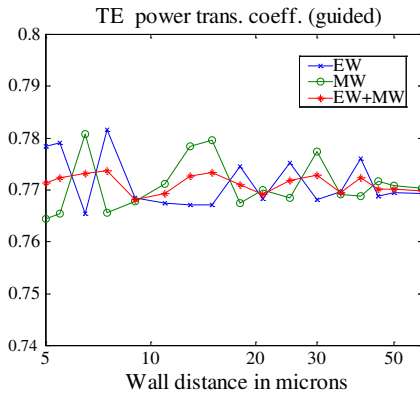
Figure 4. Convergence plot of TE guided power transmission coefficient as a function of wall separation distance.
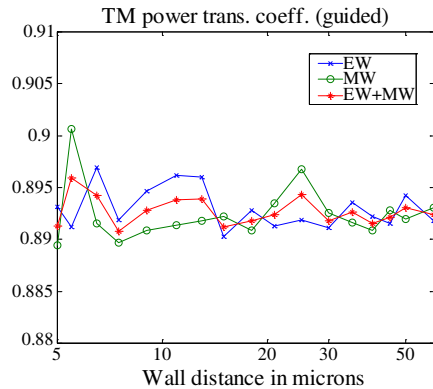
Figure 5. Convergence plot of TM guided power transmission coefficient as a function of wall separation distance.

Table 1. Comparison of power reflection and transmission coefficients between CTMIE and hybrid FD-FD method from normal to high grid/mode density. All other parameters are same as those that produce Figures 3(a) and (b).

		FD-FD $N_\lambda = 20$	FD-FD $N_\lambda = 40$	CTMIE $F_{SM} = 10$ $F_{AF} = 2$	CTMIE $F_{SM} = 25$ $F_{AF} = 5$
r_G	TE	0.1136	0.1099	0.1144	0.1156
	TM	0.1011	0.1029	0.0937	0.1007
t_G	TE	0.7672	0.7735	0.7783	0.7695
	TM	0.8661	0.8869	0.8972	0.8918
r_R	TE	0.0491	0.0365	0.0403	0.0496
	TM	0.0040	0.0045	0.0023	0.0041
t_R	TE	0.0649	0.0788	0.0670	0.0652
	TM	0.0034	0.0033	0.0069	0.0034
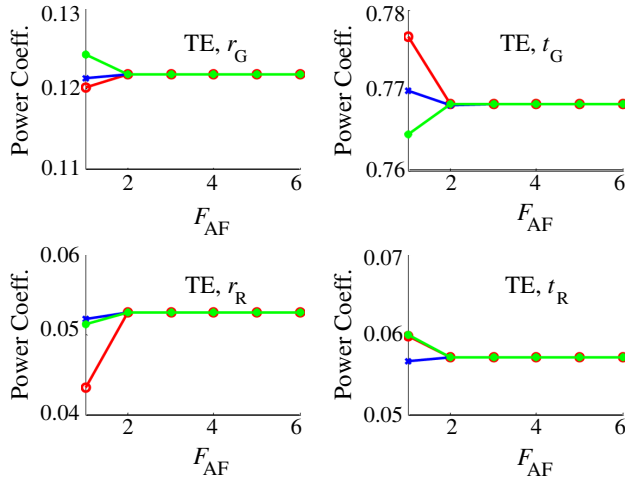
Figure 6. Convergent plot of TE polarized reflection and transmission coefficients of power (guided/radiating) for three types of auxiliary functions as function of F_{AF} parameter. Data points for trigonometric basis (TB) is shown with red circles, basis using left slicemode bases (LB) in blue crosses and right slicemode bases (RB) in green dots.
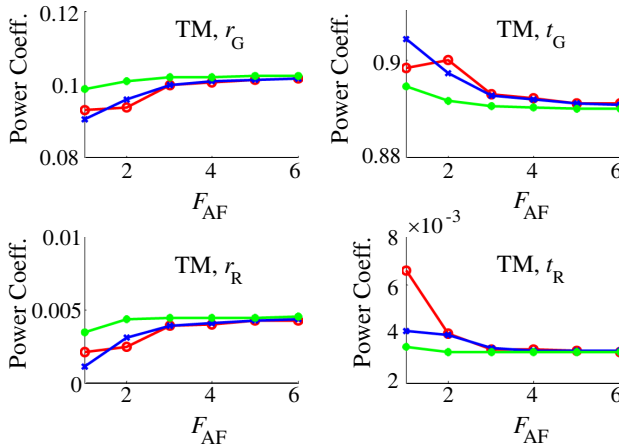
Figure 7. Convergent behavior of TM polarized reflection and transmission coefficients of guided and radiating power. Caption parameters are same as those in Figure 6.

Now we turn our attention to the AFtype parameter, the effect of choosing the auxiliary function. In Figure 6, we show convergent behavior of TE polarized, t_G as function of F_{AF} for different AFtype. Each data point is computed twice using Equation (8) (to reduce wall effects) while keeping the ratio of $F_{SM}/F_{AF} = 5$. In each subplot three curves corresponding to a AFtype of TB (red circle), LB (blue cross) and RB (green dot) are plotted. Results of TM polarization are shown in Figure 7 shows. We see dissimilar behavior from the TE case especially for those radiated power coefficients. The convergence rates are slower also.

We would like to point out the mode-matching method [13] and film mode matching [14] are related to our CTMIE formulation with AFtype tied either to the left slice modes (LB) or the right slice modes (RB). Furthermore F_{SM} is always equal to F_{AF} in both cases. While these three curves will merge into one as F_{AF} increases to some large number, we observe (not shown here) intense fluctuation for $F_{AF} \ll 1$, in the cases $F_{SM} = F_{AF}$. A detail numerical comparison between these methods is beyond the scope of this paper.

3.2. MMI 2 by 2 Power Cross Coupler

In this example, we study the multimodeinterference device (MMI) which serves as the perfect case for CTMIE applications. The simplest MMI device, illustrated in Figure 8, is the two by two power cross

coupler. It can be completely analyzed by CTMIE using just one or two unknown functions depending if the symmetry is applied or not. Both approaches will be computed to verify consistency between CTMIE equations for $N = 1$ and $N = 2$ cases.

The MMI waveguide has a width of W_{MMI} and a length of L_{MMI}. The most important parameter the coupling length L_π is defined as the beat length between the two lowest guided modes of the MMI waveguide. It is approximated by the standard mode propagation analysis (MPA) [22, 23] as:

$$L_\pi \triangleq \frac{\pi}{\beta_0 - \beta_1} \cong \frac{4n_c W_e^2}{3\lambda_0}. \tag{9}$$

where β_0 is the fundamental mode propagation constant, n_c is the MMI core index and λ_0 is the operating wavelength. The effective MMI width W_e, which is weakly polarization dependent, is slightly larger than W_{MMI}.

MMI devices are usually verified by MPA or BPM. Both types of methods ignore the reflection and higher-order modes excited by the discontinuities at input/output waveguide junctions. CTMIE includes all these effects and is the method of choice for analyzing novel MMI couplers with stepped-width design [24]. The full MMI structure of
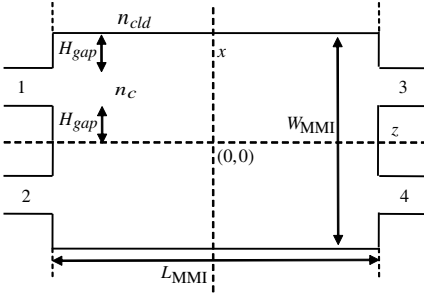
Figure 8. Illustration of the 2×2 multimode-interference power cross coupler. The core and cladding indices are n_c and n_{cld}, respectively.
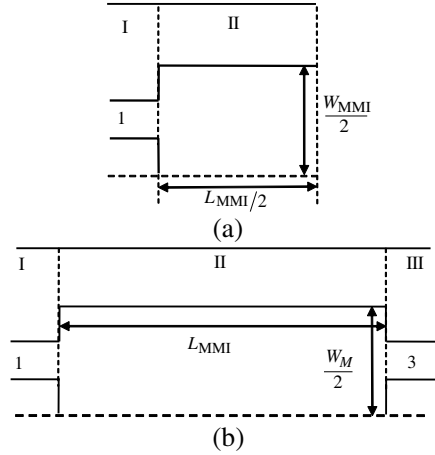
Figure 9. The symmetry structure for MMI coupler in Figure 8. (a) 1/4 structure, (b) 1/2 structure.ided power transmission coefficient as a function of wall separation distance.

Figure 8 has two-fold symmetry with respect to x and z axis. We can break the full-size problem into sub problems depicted by Figure 9. This simple MMI device will be analyzed by CTMIE with one unknown function ($N = 1$, Figure 9(a)) or with two-unknown functions ($N = 2$, Figure 9(b)).

In this case, we assume that the wavelength is $1.3\,\mu m$. The core index n_c is 3.5 and cladding index n_{cld} is 1.5, respectively. Using an MMI width $W_{\mathrm{MMI}} = 6.6\,\mu m$, the computed L_π for TE and TM modes are $162.48\,\mu m$ and $157.36\,\mu m$ respectively. MMI theory predicts that at $z = 3L_\pi$ a reverse (in x) image will appear. At this point energy from port one will be focused into port four and likewise port two energy will go to port three.

We found under our full wave analysis using $N = 1$ and $N = 2$ models, the differences in (computed) through and cross power transmission coefficients are less than 10^{-14}, that is, the two results are numerically identical. The cross power transfer coefficient is 89.80% for TE mode and 85.70% for TM mode while the TE through power transfer coefficient is 5.20% (TM, 8.03%). The reflected power coefficients are small, (0.13%/4.24%, for TE through/cross port, 2.321%/3.26% for TM through/cross port), but nonetheless can not
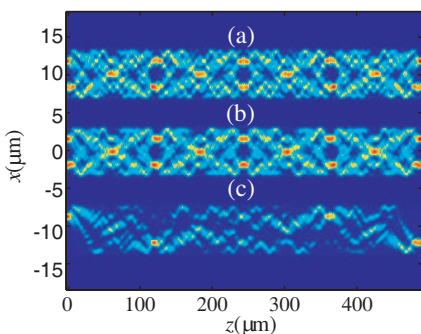
Figure 10. TE field intensity distribution in a MMI cross coupler computed with CTMIE formulation. (a) $N = 1$ with a PECW at $z = 245\,\mu m$, (b) $N = 1$ with a PMCW at $z = 245\,\mu m$, (c) Field sum of (a) and (b), but plotted as the field intensity.
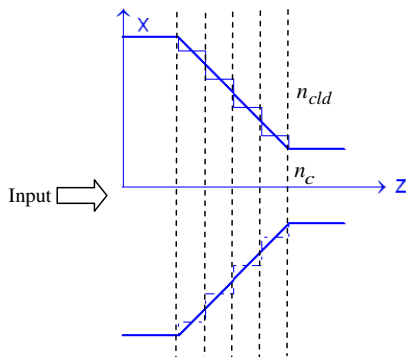
Figure 11. A 45 degree linearly tapered waveguide is first divided into N sections in the tapered region. $N = 4$ in this illustration. Note that the core-cladding interface of each slice is always chosen to be in the middle of the section.

be ignored in some applications. Due to the long device size, the field intensity distribution is shown in Figure 10 for the TE case For comparison, using MPA, the cross power transfer coefficients are 85.25% for TE mode and 80.99% for TM mode while the TE through power transfer coefficient is 6.02% (TM, 6.92%). We observed 100% power conservation under CTMIE but not under MPA.

3.3. Linearly Tapered Waveguide

For the last example, we study CTMIE for an $N \geq 3$ case. For this we choose to analyze a linearly tapered waveguide. Even though this tapered waveguide is continuous, we can apply the piece-wise stair-case approximation to the original structure by using as many 1-D horizontally layered structures (slices) as needed. The situation is further illustrated in Figure 11 where the tapered section is first divided into N sections of slices.

The field distributions of this tapered waveguide are shown in Figure 12. In this example, the refractive index $n_c = 2.5$ and $n_{cld} = 1$. The incident field is the fundamental mode of the input waveguide at the wavelength of $1.3 \, \mu m$. The core thicknesses of input/output waveguide is $1.0 \, \mu m / 0.25 \, \mu m$. The PECW wall separation distance is set at 30 and $40 \, \mu m$. The mode factor ratio F_{SM}/F_{AF} is kept at 2.

Our final goal is to investigate the effect of slicing density on the CTMIE solutions of waveguide devices with continuous profiles. In this example the transition of core thickness from $1 \, \mu m$ to $0.25 \, \mu m$ completes in a distance of $0.375 \, \mu m$ which is about three quarter of a wavelength in the core. A 50-slice approximation would amount to a
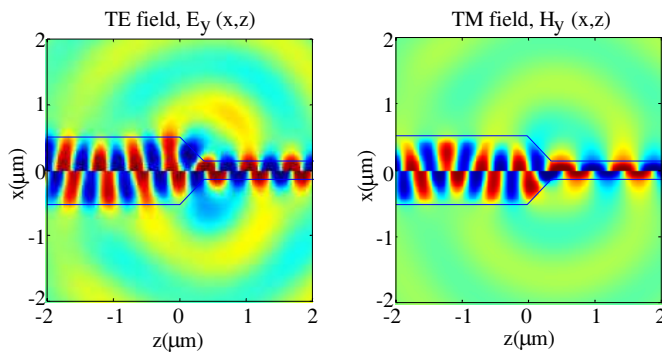
Figure 12. TE and TM field distributions in the symmetric 45 degree tapered waveguide. Real part is plotted on the upper half while the imaginary part is plotted on the lower half.
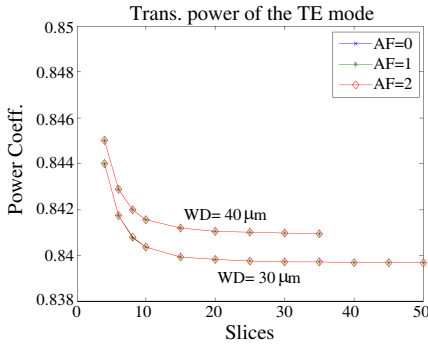
Figure 13. TE polarized, guided power transmission coefficient as function of N, number of slices in the tapered region Results for all AFtypes are virtually identical.
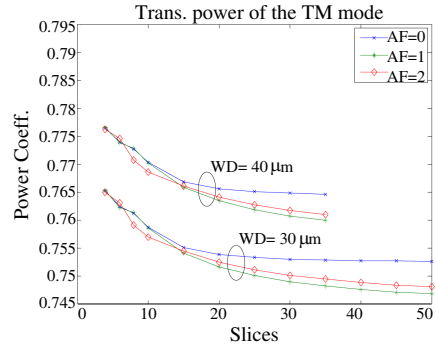
Figure 14. TM polarized, guided power transmission coefficient as function of N, number of slices in the tapered region. TM convergent rate is slower There are also some small differences in computed results for different AFtypes.

slicing density of $70/\lambda$ in the core or $175/\lambda$ in the air cladding. Again, for this purpose, we examine the computed guided power transmission coefficient as function of N. The calculation is repeated for two WD values and three auxiliary function types. The final results are plotted in Figures 13 and 14 for TE and TM polarizations. Note that this a big calculation that we ran out of memory for data points requiring more memory than our system running Matlab program under window XP with a total of 2 GB of RAM.

In this example, convergence is achieved with a low N for TE polarization using just about any AFtype. For TM polarization, due to discontinuous field derivative across the core-cladding boundaries, convergence of t_G is rather slow and depends on the particular AFtype used.

We verify four power transmission and reflection coefficients of this linearly tapered slab waveguide with the hybrid FD-FD method. Like example 1, the results agree well between the two set of computations. It is interesting to note that in the hybrid FD-FD method, we employ a polarization-dependent material averaging scheme for the FD-FD coefficients. As a result, FD-FD solutions begin to converge starting at $N_\lambda \approx 25$ for TE and at $N_\lambda \approx 45$ for TM polarization. Whereas in CTMIE a much higher slicing density is needed, because it faithfully computes the underlying stair-case profile with many sharp corners not

in the original device profile. Thus the hybrid FD-FD algorithm may be the more practical method of choice for this example.

There are many waveguide devices that we have not shown in this paper, are well-suited for analysis by the CTMIE method. Examples include waveguide discontinuities [25], Y-branch couplers, micro-ring cavities with dimension less than 50 micrometers, deep etched periodic grating structures (too difficult for CMT, coupled-mode theory), corrugated waveguides [26] and other novel devices require bi-directional full wave analysis.

4. CONCLUSIONS

In this paper, we successfully apply CTMIE theory to study passive dielectric waveguide devices used in planar lightwave circuit. We present detail numerical results using three waveguide examples to cover the entire application range of CTMIE formulation. Using previously published results, our hybrid FD-FD method and internal CTMIE verification, we validate our theory and Matlab programs for both TE and TM polarizations. We show that CTMIE is among methods of choice for rigorous analysis of medium-size complex waveguide devices.

ACKNOWLEDGMENT

REFERENCES

1. Saleh, B. E. A. and M. C. Teich, *Fundamental of Photonics*, John Wiley & Son, New York, 1991.

2. Lin, C. F., *Optical Components for Communications*, Kluwer Academic Publishing, Boston, 2004.

3. Chew, W.-C., *Waves and Fields in Inhomogeneous Media*, Van Norstrand Reinhold, New York, 1990.

4. Ishimaru, A., *Electromagnetic Propagation, Radiation, and Scattering*, Prentice Hall, Englewood Cliffs, N.J., 1991.

5. Taflove, A and S. Hagness, *Computational Electrodynamics: The Finite-difference Time-domain Method*, Artech House, Norwood, MA, 2000.

6. Chiang, Y. C., Y. Chiou, and H. C. Chang, "Improved full-vectorial finite-difference mode solver for optical waveguides with step-index profiles," *J. of Lightwave Technology*, Vol. 20, No. 8, 1609–1618, Aug. 2002.

7. Chang, H.-W and W.-C. Cheng, "Analysis of dielectric waveguide termination with tilted facets by analytic continuity method," *Journal of Electromagnetic Waves and Applications*, Vol. 21, No. 12, 1653–1662, 2007.

8. Chang, H.-W., W.-C. Cheng, and S.-M. Lu, "Layer-mode transparent boundary condition for the hybrid FD-FD method," *Progress In Electromagnetics Research*, PIER 94, 175–195, 2009.

9. Jin, J., *The Finite Element Method in Electromagnetics*, John Wiley & Son, New York, 2002.

10. Feit, M. D. and J. A. Fleck, Jr., "Light propagation in graded-index optical fibers," *Applied Optics*, Vol. 17, No. 24, 3990–3998, 1978.

11. Koch, T. B., J. Davies, and D. Wickramasinghe, "Finite element finite-difference propagation algorithm for integrated optical devices," *Electronics Letters*, Vol. 25, No. 8, 514–516, 1989.

12. Chang, H.-W. and M.-H. Sheng, "Field analysis of dielectric waveguide devices based on coupled transverse-mode integral equation — Mathematical and numerical formulations," *Progress In Electromagnetics Research*, PIER 78, 329–347, 2008.

13. Mittra, R., Y. L. Hou, and V. Jannejad, "Analysis of open dielectric waveguides using mode-matching technique and variational methods," *IEEE Trans. Microwave Theory Tech.*, Vol. 28, 36–43, 1980.

14. Sudbo, A. S., "Film mode matching: A versatile numerical method for vector mode field calculations in dielectric waveguides," *Pure Appl. Opt.*, Vol. 2, 211–233, 1993.

15. Chang, H.-W., T.-L. Wu, and M.-H. Sheng, "Vectorial modal analysis of dielectric waveguides based on coupled transverse-mode integral equation: I — Mathematical formulations," *J. Opt. Soc. Amer. A*, Vol. 23, 1468–1477, Jun. 2006.

16. Chang, H.-W. and T.-L. Wu, "Vectorial modal analysis of dielectric waveguides based on coupled transverse-mode integral equation: II — Numerical analysis," *J. Opt. Soc. Amer. A*, Vol. 23, 1478–1487, Jun. 2006.

17. Cheng, Q. and T. J. Cui, "Guided modes and continuous modes in parallel-plate waveguides excited by a line source," *Journal of Electromagnetic Waves and Applications*, Vol. 21, No. 12, 1577–

1587, 2007.

18. Chang, H.-W. and M.-H. Sheng, "Errata for the paper entitled 'Dielectric waveguide devices based on coupled transverse-mode integral equation — Mathematical and numerical formulations'," *Progress In Electromagnetics Research C*, Vol. 8, 195–197, 2009.

19. Rostami, A. and H. Motavali, "Asymptotic iteration method: A powerful approach for analysis of inhomogeneous dielectric slab waveguides," *Progress In Electromagnetics Research B*, Vol. 4, 171–182, 2008.

20. Motavali, H. and A. Rostami, "Exactly modal analysis of inhomogeneous slab waveguide using nikiforov-uvarov method," *Journal of Electromagnetic Waves and Applications*, Vol. 22, No. 5–6, 681–692, 2008.

21. Wu, T.-L. and H.-W. Chang, "Guiding mode expansion of a TE and TM transverse-mode integral equation for dielectric slab waveguides with an abrupt termination," *J. Opt. Soc. Amer. A*, Vol. 18, 2823–2832, Nov. 2001.

22. Soldano, L. B. and E. Pennings, "Optical multi-mode interference devices based on self-imaging: Principles and applications," *J. of Lightwave Technology*, Vol. 13, 615–627, 1995.

23. Bachmann, M., P. Besse, and H. Melchior, "Overlapping-image multimode interference couplers with a reduced number of self-images for uniform and nonuniform power splitting," *Applied Optics*, Vol. 34, 6898–6910, Oct. 1995.

24. Feng, J.-Y., P. Chang, T. Lay, and T. Chang, "Novel stepped-width design concept for compact multimode-interference couplers with low cross-coupling ratio," *IEEE Photonics Tech. Letters*, Vol. 19, No. 4, 224–226, Feb. 2007.

25. Lilonga-Boyenga, D., C. N. Mabika, and G. Okoumou-Moko, "Rigorous analysis of uniaxial discontinuities microwave components using a new multimodal variational formulation," *Progress In Electromagnetics Research B*, Vol. 2, 61–71, 2008.

26. Liao, S., "Miter bend mirror design for corrugated waveguides," *Progress In Electromagnetics Research Letters*, Vol. 10, 157–162, 2009.